Nuclear Engineering and Design 388 (2022) 111628

Contents lists available at ScienceDirect

Nuclear Engineering and Design

journal homepage: www.elsevier.com/locate/nucengdes

Point-kinetics neutron noise modeling and analysis via probabilistic finite state automata

Xiangyi Chen [a], Asok Ray [b,*], Fan Zhang [c]

[a] Department of Nuclear Engineering, Pennsylvania State University, University Park, 16802 PA, USA
[b] Departments of Mechanical Engineering, Nuclear Engineering and Mathematics, Pennsylvania State University, University Park, 16802 PA, USA
[c] Nuclear and Radiological Engineering and Medical Physics, Georgia Institute of Technology, Atlanta, 30316 GA, USA

A B S T R A C T

This paper addresses two issues for safety & performance analysis of nuclear reactors; these issues are: (i) Modeling of the neutron noise process, which is constructed as stochastic differential equations by augmenting deterministic dynamic models of point kinetics, thermal hydraulics, and mechanical vibrations in the reactor core, and (ii) Time-series analysis of nuclear reactor internals for early-stage anomaly detection by making use of the neutron noise model. The model is used to generate an ensemble of time series of neutron noise under both normal and anomalous operating conditions, where an anomaly in the postulated probability distribution of neutron noise is caused by abnormal vibration of the fuel assembly. A symbolic time series analysis (STSA) tool, called probabilisitc finite state automata (PFSA), has been selected to detect the anomalies, if any. The PFSA method symbolizes a time-series and then encodes the resulting symbol string into a state transition probability matrix, which is both stochastic and ergodic by construction. The discrimination function for anomaly detection is built upon the residual error of the principal (left) eigenvector of the state transition probability matrix, which is also the state probability vector of the PFSA. The accuracy of the proposed analysis and its capability for online anomaly detection is demonstrated by simulation on a low-order dynamic model of a 2,500 MWt PWR of the Three-Mile-Island type.

1. Introduction

Neutron noise is a consequence of fluctuations in the neutron flux of the reactor core around the trend values. The rich information contained in the neutron noise can be extracted for diagnostics and surveillance of a nuclear reactor. For example, the neutron noise spectrum along with other signals are measured in the four-loop pressurized water reactor (PWR) plants, built by Kraftwerk Union AG (KWU), to identify the frequencies of mechanical vibrations, degradation signatures, and anomalous behavior (Seidl et al., 2015). The neutron noise is also expected to serve as a source of important information for predictive maintenance and prognostics of the next generation small modular reactors (Meyer et al., 2013). For the reactors under development, which are featured with ultra-long refueling cycle, such prognostics tools are especially important to guarantee the plant availability and safety. Another example is the BORIS reactor, proposed in South Korea, which has an interval of one fuel cycle of more than 20 years (Lee et al., 2006), and therefore the predictive maintenance dominates all maintenance regimes. Since the routes of neutron noise are directly related to the health of reactor core internals, the analysis of neutron noise is a significant part in the health & usage monitoring system (HUMS). Examples of the well-known sources of neutron noise are:

- Vibrations in the fuel assembly, control rods, and supporting structures, as well as rotational machinery in the primary side of the nuclear plant.
- Fluctuations in the fluid flow, pressure, density, and void fraction of the reactor coolant.
- Random processes generated by fission reaction and neutron detection.

In practice, the information generated from time series of neutron noise is usually structured in the form of power spectral density (PSD), where the distinct peaks on the spectra can be explained in different ways.

As an example, the analysis (Trenty et al., 1991) on the feature peaks of the PSD recorded by the ex-core detectors of Électricité de France (EDF) reactors are summarized below:

- **0.5–2.0 Hz band**: Thermal–hydraulic fluctuations.
- **2.0–5.0 Hz band**: First beam mode of the fuel assembly.
- **5.0–7.5 Hz band**: Second beam mode of the fuel assembly.
- **7.5–10.0 Hz band**: Core barrel free swinging. The core barrel is clamped at the reactor vessel flange and vibrate laterally like a beam (Thie, 1979).

* Corresponding author.
E-mail addresses: xxc90@psu.edu (X. Chen), axr2@psu.edu (A. Ray), fan.zhang@me.gatech.edu (F. Zhang).

https://doi.org/10.1016/j.nucengdes.2021.111628
Received 21 September 2021; Received in revised form 10 December 2021; Accepted 20 December 2021
Available online 28 January 2022

- **14.0–18.0 Hz band**: Vessel swinging around the primary coolant pipes.
- **18.0–24.0 Hz band**: Shell mode n = 2 of the core barrel. The shell modes are the vibration changing the internal area or circumferential shape (Thie, 1979).
- **26.0–48.0 Hz band**: Sensor background noise and complex modes of internals.

The above analysis has been performed on a database for vibration monitoring of PWR internals. With the one-to-one correspondence between the feature peaks and the sources, it appears that PSD analysis can be used for anomaly detection and classification of the reactor internals. Consequently, many methods of neutron noise analysis for monitoring of reactor internals have been developed in the frequency domain, based on PSD analysis (Schoonewelle et al., 1996; Zwingelstein and Upadhyaya, 1979; Alguindigue et al., 1993). Apparently, there is a lack of data-driven analysis methods that are based on direct usage and analytical derivation of time series information to both transient and stationary operations.

Since generation of time series data is expensive and such data are not easily accessible, a viable alternative is to develop a neutron-noise model for data generation and construction of associated analytical methods. There are two main ways of developing the simulation model.

In the first way, vibration models are integrated into the available core simulators (e.g., the S3K (Chionis et al., 2020), DYN3D (Viebach et al., 2019) & CORE SIM (Demaziere, 2011)), and the associated space-dependent problems are addressed. Based on the simulated space-dependent data traditional frequency domain methods and state-of-the-art pattern recognition methods are applied to understand the neutron noise phenomenology. The traditional frequency domain methods usually make use of: (a) the auto-power spectral density (APSD) for a single signature, (b) the cross-power spectral density (CPSD) between signatures at different positions, and (c) the coherence which is a function of APSD and CPSD. The state-of-the-art pattern recognition methods are also explored, especially in the CORTEX project [1]. Some example references are (Demazière et al., 2021; Durrant et al., 2021; Durrant et al., 2019). The references (Demazière et al., 2021; Durrant et al., 2019) apply the principle of 3-dimensional Convolutional Neural Network (CNN) for identification of various anomaly scenarios in frequency domain. The reference (Durrant et al., 2019) also applies the long short term memory (LSTM) for the time series data generated by the S3K code. Reference (Durrant et al., 2021) uses the voxel-wise, fully-convolutional, semantic segmentation network for detection and isolation of multiple and simultaneously occurring perturbations and anomalies. To accommodate the difference between the simulated data and the real nuclear power plant data, the unsupervised domain adaptation technique is applied to align the learned representation of the feature spaces of the simulated data and true data (Durrant et al., 2021). This attempt represents the state-of-the-art in the neutron noise analysis technique and the AI techniques in nuclear anomaly detection & isolation.

The second way, which has so far been studied to a rather limited extent, uses state-space modeling. The state-space model could be detailed enough to study parts of the phenomena as what can be done by using simulators. For example, in reference (Shieh et al., 1987), the neutron-noise analysis is conducted to study the moderator temperature coefficient of reactivity in the frequency domain. Alternatively, the state-space model could be simple enough to identify the noise term (Dubi and Atar, 2021). The benefit of using the state-space model is that it is fast in simulation and can be easily adapted to different scenarios. However, the related studies in history usually include limited mechanisms of neutron noise, thus the time series data generated drops many main features of real power plants. Therefore, these data are inadequate in time domain analysis for anomaly detection. To conduct the time-domain analysis, two conditions on the simulated data should be satisfied: (i) the spectrum features from ∼ 0–20 Hz (which is of interest) should be embedded in the time series; and (ii) the computation should be fast enough to obtain the simulation results over a relatively long time period with a small time step (e.g., ∼milliseconds) of integration. This work aims to address the issues of neutron-noise modeling and analysis in the setting of state-space time series.

Contributions: Major contributions and implications of the work reported in this paper are summarized below.

1. *Neutron noise modeling under nominal operating conditions as well as under postulated abnormal fuel assembly vibrations*: The neutron-noise model is built upon the base model, which includes stochastic differential equations (SDEs) of neutron point kinetics, and ordinary differential equations of thermal–hydraulics developed in reference (Dubi and Atar, 2021). The neutron-noise model shows good description of the detector response and components' vibration models. The anomaly at an early stage does not cause the neutron noise amplitude to change but is with low frequency spectrum variation. The proposed modeling method can be adapted and extended to simulate other possible anomalies (e.g., equivalent to modifying and/or including more feature peaks in the PSD).
2. *Development of a time-domain machine learning (ML) tool for early state anomaly detection in nuclear reactors*: The statistical ML tool, adopted here, is probabilistic finite state automata (PFSA) (Ray, 2004; Mukherjee and Ray, 2014) that has been successfully used for anomaly detection & classification in different applications (e.g., Ghalyan and Ray, 2021; Ghalyan and Ray, 2020) although this paper is apparently the first reported usage of PFSA in nuclear engineering applications.

Organization: The paper is organized in five sections including the present one. Section 2 develops the model to simulate neutron noise. Section 3 succinctly presents the machine learning (ML) tool, called probabilistic finite state automata (PFSA), for anomaly detection. Section 4 describes how the neutron noise simulation is conducted and presents the results of PFSA-based anomaly detection. Section 5 concludes the significance of the reported work along with recommendations for future research.

2. Neutron-noise Modeling for Simulation

This section develops nonlinear stochastic differential equations for neutron-noise simulation. It is recognized that the probability distribution of neutron noise is non-stationary in the sense that it varies with the burnup during the fuel cycles within the reactor lifetime as well as with operating conditions. The model developed in this section does not consider these perturbations. It is also noted that the model only represents a generic PWR reactor and that the model is limited to vibrations of specific reactor components and thermal–hydraulic fluctuations in the primary coolant only. However, the model can be extended to include other phenomena of interest.

2.1. Reactor point kinetics and thermal hydraulics models

The non-stochastic equations of point kinetics including the dynamics of prompt neutrons and one-delay group are stated below.

$$\frac{dn(t)}{dt} = \left(\frac{\rho(t)-\beta}{\Lambda}\right) n(t) + \lambda\, c(t), \tag{1}$$

$$\frac{dc(t)}{dt} = \left(\frac{\beta}{\Lambda}\right) n(t) - \lambda\, c(t). \tag{2}$$

The variables and parameters of the above and following equations are reported in Table 1, where the values of these parameters (Edwards et al., 1990) represent a 2500 MWt PWR of the Three Mile Island-type.

[1] https://cortex-h2020.eu

Table 1
Nomenclature and values of system parameters

Symbols	Quantity	Values
n	neutron density	-
c	delayed neutron precursor's concentration	-
n_r	relative neutron density	$n_r(0) = 1$
c_r	delayed neutron precursor's relative concentration	$c_r(0) = 1$
$P_a\|_{ss}$	steady state reactor power	2500 [MW]
f_f	fraction of reactor power deposited in the fuel	0.98
λ	effective precursor decay constant	0.125 [s^{-1}]
Λ	effective prompt neutron lifetime	0.0001 [s]
β	delayed neutron fraction	0.0065
α_c	coolant temperature coefficient	0.00001 [K^{-1}]
α_f	fuel temperature coefficient	−0.00005 [K^{-1}]
Ω	heat transfer coefficient between fuel and coolant	6.53 [MW K^{-1}]
M	mass flow rate times heat capacity of coolant water	92.8 [MW K^{-1}]
μ_f	total heat capacity of the fuel and structural material	26.3 [MW s K^{-1}]
μ_c	total heat capacity of the reactor coolant	70.5 [MW s K^{-1}]
T_h	hot leg temperature	$T_h(0) = 590.09$ [K]
T_c	cold leg temperature	563.15 [K]
T_f	average fuel temperature in the reactor	$T_f(0) = 965.28$ [K]
ρ	overall reactivity insertion	$\rho(0) = 0$
ρ_r	control rod reactivity insertion	$\rho_r(0) = 0$

Remark 1. The one-group model of delayed neutron's precursors has been used in this paper to save the computation time and memory of the simulation. The authors envisage that the methods developed in this work are also feasible to construct models of a larger number (e.g., up to 6) of delayed neutron groups. A singularly perturbed model could also be used to further save the computation time (Chen et al., 2020).

At a steady state (ss), having the total reactivity $\rho_{ss} = 0, \frac{dn(t)}{dt}|_{ss} = 0$, and $\frac{dc(t)}{dt}|_{ss} = 0$, it follows from Eq. (2) that:

$$\frac{c|_{ss}}{n|_{ss}} = \frac{\beta}{\lambda\Lambda}. \tag{3}$$

After normalizing the neutron density and precursor concentration with respect to their steady state values, Eqs. (1) and (2) are rewritten as:

$$\frac{dn_r(t)}{dt} = \left(\frac{\rho(t) - \beta}{\Lambda}\right) n_r(t) + \left(\frac{\beta}{\Lambda}\right) c_r(t), \tag{4}$$

$$\frac{dc_r(t)}{dt} = \lambda n_r(t) - \lambda c_r(t). \tag{5}$$

The thermal–hydraulics model uses two energy balance equations for the reactor fuel and the primary coolant:

$$\frac{dT_f}{dt} = \frac{f_f P_a|_{ss} n_r(t) - \Omega(T_f - T_h)}{\mu_f}, \tag{6}$$

$$\frac{dT_h}{dt} = \frac{(1 - f_f) P_a|_{ss} n_r(t) + \Omega(T_f - T_h) - M(T_h - T_c)}{\mu_c}, \tag{7}$$

and the total reactivity due to external reactivity insertion (e.g., fuel assembly vibration) and temperature feedback from the coolant and fuel is:

$$\rho(t) = \rho_e(t) + \alpha_f\big(T_f(t) - T_f(0)\big) + \alpha_c(T_h(t) - T_h(0)). \tag{8}$$

The stochastic neutron point kinetics and stochastic thermal hydraulics are modeled by augmenting Eqs. (4)–(8) with additive and parametric noise (Konno et al., 1989). The assumptions made here are as follows:

1. The white Gaussian noise $F_N(t)$ is added to the differential equation of the neutron density (Eq. (4)) accounting for the complex sources of neutron noise. This assumption is made based on the fact that the central limit theorem is applicable to the cumulative effects of a large number of independent and identically distributed (iid) neutron population. It is noted that the integral (in the mean-square sense) of the white Gaussian noise is the Brownian motion with the power spectral density $\sim \frac{1}{f^2}$ (Krapf et al., 2018), where f is the frequency; this relation satisfies the fact that the observed base spectrum of neutron noise approximately follows the power-law distribution in a wide range of the frequency domain.
2. The colored Gaussian noise $\varepsilon_T(t)$ is added to the differential equation of the coolant temperature (Eq. (7)) accounting for the temperature fluctuations of the coolant. This assumption is based on the fact that the low-frequency region of the PSD spectrum, corresponding to the peak response of thermal–hydraulic oscillations, has the dominant power (Torres et al., 2019).
3. The colored parametric noise $\rho_e(t)$ is introduced by the random reactivity insertion (and withdrawal) due to the fuel assembly vibration.

The colored parametric noise $\rho_e(t)$ and additive noise $\varepsilon_T(t)$ are the response of the vibration filters described in the following subsections.

2.2. Fuel assembly vibration model and in-core detector signal

Under the normal operation, vibration of the fuel assembly is modeled by a linear time-invariant (LTI) single degree of freedom (SDOF) oscillator with Gaussian white noise excitation (Preumont, 2013). However, the oscillations could become nonlinear upon occurrence of an anomaly (Konno and Saito, 1984; Konno, 1986). A potential term $V(\varepsilon_a)$ with an order equal to or greater than 3 can be used to model this nonlinearity (Konno and Saito, 1984). Thus, the vibration model of the displacement ε_a (Preumont, 2013) is:

$$\ddot{\varepsilon}_a + 2\xi\omega_n\dot{\varepsilon}_a + \frac{\partial}{\partial\varepsilon_a}V(\varepsilon_a) = F_a(t), \tag{9}$$

where the potential $V(\varepsilon_a)$ is expressed as:

$$V(\varepsilon_a) = \sum_{n=1}^{N} \frac{A_n}{n}\varepsilon_a^n, \tag{10}$$

and the potential is induced by the force $U(\varepsilon_a)$ as:

$$U(\varepsilon_a) = \frac{\partial V(\varepsilon_a)}{\partial\varepsilon_a} = A_1 + A_2\varepsilon_a + A_3\varepsilon_a^2 + \ldots + A_N\varepsilon_a^{N-1}. \tag{11}$$

The excitation force $F_a(t)$ is primarily induced by the turbulent pressure on the interacting surfaces. The fuel rods have large surface areas though, but the forces are generally balanced. The primary reason of the vibration could be the mixing vane patterns of the grid spacer (Kim and Suh, 2008). The mixing vane is used to enhance the turbulence to assure the capability of supporting the random opposite reaction force by itself, where white Gaussian excitation noise is assumed. Since the vibration model is assumed to be linear, the response is also Gaussian but it is colored. In the absence of an anomaly, the $U(\varepsilon_a)$ term is a linear function of the displacement, i.e., $A_1 = A_3 = \cdots A_N = 0$ and $A_2 = \omega_n^2$ is a constant. Then, the Eq. (9) is reduced to

$$\ddot{\varepsilon}_a + 2\xi\omega_n\dot{\varepsilon}_a + \omega_n^2\varepsilon_a = F_a(t). \tag{12}$$

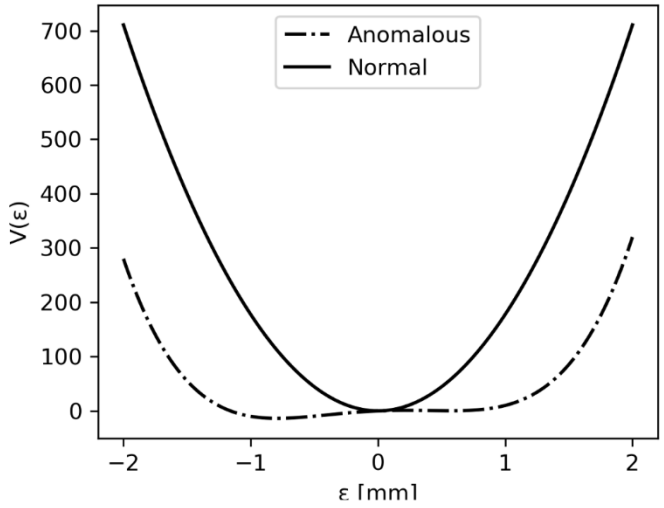

Fig. 1. Potential functions for normal and anomalous fuel assembly vibration.

The power spectral density (PSD) of the response of the above oscillator is:

$$\Phi_{\varepsilon\varepsilon}(\omega) \propto \frac{1}{\left(\omega_n^2 - \omega^2\right)^2 + 4\xi^2\omega^2\omega_n^2}. \tag{13}$$

The natural frequency ω_n is the oscillation frequency (unit: rad/s) of a free undamped oscillator. With white Gaussian excitation, the natural frequency determines the location of the peak on the PSD for an undamped oscillator. In a lightly damped system, the maximum frequency of the transmissibility is achieved when the frequency of the applied load is close to the natural frequency. The damping ratio, ξ, along with the natural frequency determines the height of the peak on PSD. An undamped system has infinite high peak. The natural frequency $f_n = \frac{\omega_n}{2\pi} \approx 3$ Hz is used for the above SDOF model accounting for the first beam mode of the fuel assembly. Another SDOF model with $f_n \approx 0.5$ Hz is used for thermal hydraulic fluctuations (e.g., temperature variations) observed on the recorded PSD diagram in the nuclear power plant:

$$\ddot{\varepsilon}_T + 2\xi\omega_{nT}\dot{\varepsilon}_T + \omega_{nT}^2\varepsilon_T = F_T(t). \tag{14}$$

The relation of the frequencies of damped vibration (ω_d) and undamped natural frequency (ω_n) (Singiresu, 1995) is:

$$\omega_d = \sqrt{1-\xi^2}\ \omega_n. \tag{15}$$

When the system is very lightly damped, i.e., $\omega_d \approx \omega_n$, which is the case here, the signals of vibrations and fluctuations can be correlated to each other. This coupling effect is not considered; otherwise they would be cross-correlated.

In the presence of an anomaly, the $U(\varepsilon_a)$ has higher order terms of ε_a. Under these circumstances, A_1 is non-zero, which is caused by the existence of a limiter, and $A_2 < 0$ that is explained by the interaction of fluid motion and the loss of cramped boundary conditions (Konno et al., 1989). It is also assumed that $A_i = 0$ for all $i > 4$ and $i = 3$ under anomaly occurrence and $A_4 > 0$, because $A_4 > 0$ guarantees a stable potential function, which means that the energy barrier is infinitely high; otherwise there is a possibility of displacement going to infinity when the potential barrier is crossed with energy in the excitation. For example, the potential function having $A_4 < 0$ could be a type of component malfunction, which is easy to be detected but it is out of the scope of early anomaly detection, reported here.

Fig. 1 shows a comparison of the potential functions in normal and anomalous vibrations of the fuel assembly. The damping ratio ξ_a is

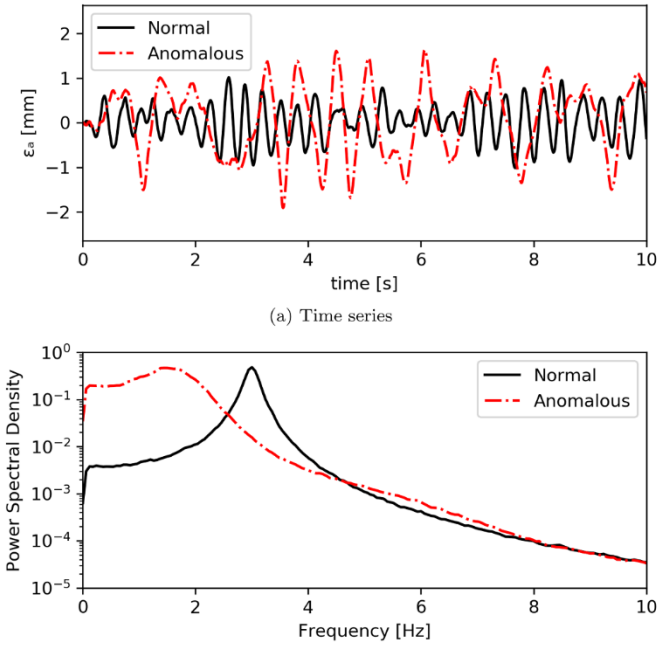

(a) Time series

(b) Power spectral density (PSD)

Fig. 2. Normal & anomalous fuel-assembly vibration.

chosen to be 0.05. The anomalous potential function has the parameters of $A_1 = 10, A_2 = -50, A_3 = 0,$ and $A_4 = 100$, which is an asymmetric double-well function (Konno, 1986). The simulated displacements and PSDs estimated by Welch's method (Welch, 1967) are shown in Fig. 2, where the red dash-dot line shows the anomalous vibration of the fuel assembly and the black solid line is the normal vibration of the fuel assembly. The spectrum of the anomalous fuel assembly vibration has lower frequency of the peak power location and the spreading of the peak is much wider than the normal fuel assembly vibration.

To connect the first beam mode of displacement of the fuel assembly with reactivity insertion, it is assumed that the displacement ε_a has the following linear relationship with the reactivity insertion:

$$\rho_e(t) = \eta\frac{d\rho}{d\varepsilon_a}\varepsilon_a(t) = b_1\varepsilon_a(t), \tag{16}$$

where $b_1 \triangleq \eta\frac{d\rho}{d\varepsilon_a}$; $d\rho/d\varepsilon_a$ is reactivity worth of the rod per unit length; and η is a conversion factor that relates the inserted reactivity associated with the axial displacement to the reactivity brought in by the displacement in the model generalized direction. So far, the models represented by Eqs. (4)–(8) are complete to calculate the dynamics of relative neutron density. The dynamics of the relative neutron density is assumed to be the same as the dynamics of noise detected by the central core neutron detector. Adding white Gaussian noise $F_N(t)$ to Eq. (4), and rearranging the neutron kinetics, thermal hydraulics and vibration models of the fuel assembly and thermal–hydraulic fluctuations, the following dynamical system with random fluctuation terms are reached,

$$\frac{d\mathbf{x}}{dt} = A\mathbf{x} + N + F, \tag{17}$$

where

$$\mathbf{x} = [n_r, c_r, T_f, T_h, \varepsilon_a, \dot{\varepsilon}_a, \varepsilon_T, \dot{\varepsilon}_T]^{\mathrm{T}},$$

$$A=\begin{bmatrix} A_{11} & \frac{\beta}{\Lambda} & 0 & 0 & 0 & 0 & 0 & 0 \\ \lambda & -\lambda & 0 & 0 & 0 & 0 & 0 & 0 \\ \frac{f_f P_a|_{ss}}{\mu_f} & 0 & -\frac{\Omega}{\mu_f} & \frac{\Omega}{\mu_f} & 0 & 0 & 0 & 0 \\ \frac{(1-f_f)P_a|_{ss}}{\mu_c} & 0 & \frac{\Omega}{\mu_c} & -\frac{\Omega+M}{\mu_c} & 0 & 0 & 1 & 0 \\ 0 & 0 & 0 & 0 & 0 & 1 & 0 & 0 \\ 0 & 0 & 0 & 0 & -A_2 & -2\xi_a\omega_{na} & 0 & 0 \\ 0 & 0 & 0 & 0 & 0 & 0 & 0 & 1 \\ 0 & 0 & 0 & 0 & 0 & 0 & -\omega_{nT}^2 & -2\xi_T\omega_{nT} \end{bmatrix},$$

$A_{11}=\frac{-\beta-\alpha_f T_f(0)-\alpha_c T_h(0)}{\Lambda}$,

$N=\left[N_1, 0, 0, \frac{T_c M}{\mu_c}, 0, -A_1-A_3\varepsilon_a^2-A_4\varepsilon_a^3, 0, 0\right]^{\mathrm{T}}$, $N_1=\frac{b_1\varepsilon_a+\alpha_f T_f+\alpha_c T_h}{\Lambda}n_r$, and $F=[F_N(t), 0, 0, 0, F_a(t), 0, F_T(t)]^{\mathrm{T}}$. On the right-hand-side of Eq. (17), the first term is the linear term; the second term is the nonlinear term and the third term is the random excitation term. Eq. (17) is written in the standard SDE form as:

$$d\mathbf{x}(t)=a(\mathbf{x}(t),t)dt+b(\mathbf{x}(t),t)dB(t), \tag{18}$$

where $a(\mathbf{x}(t),t)=A\mathbf{x}+N$, $b(\mathbf{x}(t),t)=\mathrm{diag}(\sigma_n, 0, 0, 0, 0, \sigma_a, 0, \sigma_T)$, and $dB(t)=[dB_1,\ldots,dB_8]^{\mathrm{T}}$, which is a vector of increments of Brownian motion.

2.3. Core barrel & pressure vessel vibration model and ex-core detector signal

Similar to the fuel assembly, the core barrel & pressure vessel free-swinging under normal operation is modeled by the two-degree-of-freedom (TDOF) linear time-invariant (LTI) oscillator with displacement in the same direction. Fig. 3 depicts a schematic of the pressure vessel & core barrel model.

Referring to the vibration model, Newton's 2^{nd} law yields:

$$m_1\ddot{\varepsilon}_1+c_1\dot{\varepsilon}_1+c_2(\dot{\varepsilon}_1-\dot{\varepsilon}_2)+k_1\varepsilon_1+k_2(\varepsilon_1-\varepsilon_2)=F_1(t), \tag{19}$$

$$m_2\ddot{\varepsilon}_2+c_2(\dot{\varepsilon}_2-\dot{\varepsilon}_1)+k_2(\varepsilon_2-\varepsilon_1)=F_2(t), \tag{20}$$

where m_i's are inertia, c_i's are damping factors, k_i's are stiffness, ε_i's are generalized displacements of the pressure vessel and core barrel indexed by 1 and 2, respectively. Eqs. (19) and (20) are rewritten in matrix forms as:

$$M\ddot{\boldsymbol{\varepsilon}}+C\dot{\boldsymbol{\varepsilon}}+K\boldsymbol{\varepsilon}=\boldsymbol{F} \tag{21}$$

where $M=\begin{bmatrix} m_1 & 0 \\ 0 & m_2 \end{bmatrix}$, $C=\begin{bmatrix} c_1+c_2 & -c_2 \\ -c_2 & c_2 \end{bmatrix}$, $K=\begin{bmatrix} k_1+k_2 & -k_2 \\ -k_2 & k_2 \end{bmatrix}$, $\boldsymbol{\varepsilon}=\begin{bmatrix} \varepsilon_1 \\ \varepsilon_2 \end{bmatrix}$, $\boldsymbol{F}=\begin{bmatrix} F_1 \\ F_2 \end{bmatrix}$.

The natural frequencies of undamped free-vibration are the solutions of the characteristic equation:

$$\det(K-\omega^2 M)=0. \tag{22}$$

For each natural frequency ω_i, its corresponding eigenvector of $(K-\omega^2 M)$ is called the mode shape. Under special initial conditions, the free undamped system vibrates on one of the normal modes, which is the displacement vector in the direction of one of the eigenvectors. In most cases, the system vibrates as the superposition of this two normal modes. Eq. (21) is usually decoupled to two independent equations to the normal modes by coordinates transform. This transform is not used here, but Eq. (21) is directly used to obtain the simulated displacements. Letting $\boldsymbol{y}=[\varepsilon_1,\varepsilon_2,\dot{\varepsilon}_1,\dot{\varepsilon}_2]$, Eq. (21) is re-written as:

$$\dot{\mathbf{y}}=\begin{bmatrix} \mathbf{0} & \mathbf{I} \\ -\mathbf{M^{-1}K} & -\mathbf{M^{-1}C} \end{bmatrix}\mathbf{y}+\mathbf{M^{-1}}\begin{bmatrix} 0 \\ 0 \\ F_1 \\ F_2 \end{bmatrix}. \tag{23}$$

Or in standard SDE form as Eq. (18), then $\boldsymbol{a_{CV}}=\begin{bmatrix} \mathbf{0} & \mathbf{I} \\ -\mathbf{M^{-1}K} & -\mathbf{M^{-1}C} \end{bmatrix}$, $\boldsymbol{b_{CV}}=\mathbf{M^{-1}}\mathrm{diag}(0,0,\sigma_V,\sigma_C)$. The values of the parameters used here are:

$$\boldsymbol{a_{CV}}=\begin{bmatrix} 0 & 0 & 1 & 0 \\ 0 & 0 & 0 & 1 \\ -11000.0 & 411.8 & -19.4 & 1.8 \\ 2916.7 & -2916.7 & 12.5 & -12.5 \end{bmatrix},$$

$\boldsymbol{b_{CV}}=\mathrm{diag}(0,0,1.4,1.4)$. It is noted that the above parameters have not yet been obtained from a real-life nuclear plant; instead, these are used for conceptual demonstration. To best reflect the situation of the real power plant, the parameters of $\mathbf{a}_{CV}$ as well as the intensity of random activation forces used in Eqs.(23) and (18) are chosen to capture the feature peaks of the PSD of the model and the typical PSD of real power

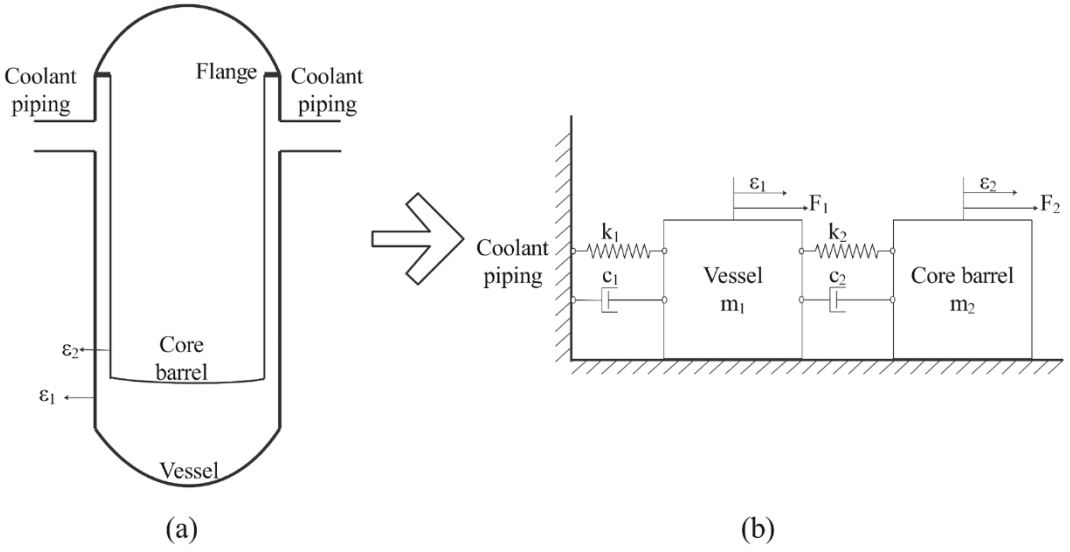

Fig. 3. Pressure vessel & core barrel modeled as a TDOF oscillator.

plants. In practice, the manufacturers obtain the parameters through mechanical tests.

The neutron noise recorded by ex-core detectors and the in-core detectors are different (Thie, 1979). In contrast to the neutron flux recorded by in-core detector at the core center, the neutron flux recorded by the ex-core detectors show higher relative power at the free swinging frequency of core barrel and supporting structure. This is caused by the relative movement of the core center to the ex-core detector. The vibration mechanism, not included in the in-core detector, should be included in the ex-core detector. It is noted that the in-core detectors close to the core-barrel are also sensitive to its vibration. The neutron flux at the position of the ex-core detector may be described by one-dimensional neutron attenuation relation (Thie, 1979). This relation is written as:

$$n_{er} = \Gamma\, n_r n(0) e^{-\mu d}, \tag{24}$$

where n_{er} is the relative neutron flux at the ex-core detector; Γ is the conversion factor of the neutron density at the reactor core to the neutron flux in the direction of the ex-core neutron detector; d is the distance from the reactor core center to the ex-core detector; and μ is the average macroscopic cross-section with the value around 0.4mm^{-1}.

Let us denote $d = d_0 + \varepsilon_2$, where d_0 is the mean distance from the reactor core center to the ex-core detector, and ε_2 is the displacement of the core barrel such that $\varepsilon_2 \ll d_0$. Normalization of n_{er} with respect to its steady-state value yields the signature recorded by the ex-core detector. Then, it follows that

$$n_{er} = \frac{\Gamma\, n_r n(0) e^{-\mu d}}{\Gamma\, n(0) e^{-\mu d_0}} = n_r e^{-\mu \varepsilon_2} \approx n_r(1 - \mu\varepsilon_2). \tag{25}$$

Fig. 4 shows profiles of time series and power spectral density of typical vibration data in the core barrel and pressure vessel.

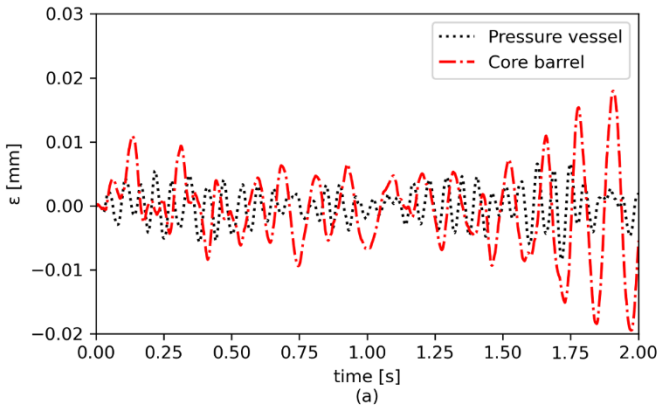

(a) Time series

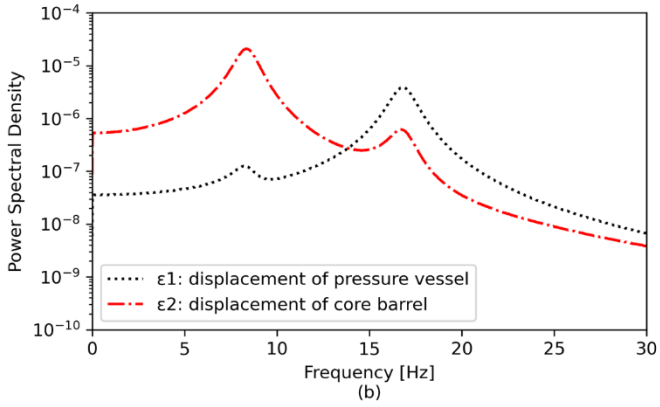

(b) Power spectral density (PSD)

Fig. 4. Typical core barrel and pressure vessel vibration data.

3. Probabilistic Finite State Automata

This section is devoted to construction of probabilistic finite state automata (PFSA) from an ensemble of time-series data. A (finite-length) time series is converted into a symbol string by partitioning the signal space into a finite number of cells, where the number of cells is identically equal to the cardinality $|\mathscr{A}|$ of the (symbol) alphabet $\mathscr{A}$, and each cell is assigned exactly one of the symbols in $\mathscr{A}$. At a given instant of time, a data point is assigned the symbol corresponding to the cell within which the data point is located; details are reported by Mukherjee and Ray (2014). The resulting symbol string is used to construct a D-Markov model, defined in SubSection 3.1, which models the statistics of the underlying stochastic process. The following definitions, which are available in standard literature (e.g., Ray, 2004; Mukherjee and Ray, 2014), are recalled here for completeness of the paper and ease of readability.

Definition 1. A finite state automaton (FSA) G, having a deterministic algebraic structure, is a triple $(\mathscr{A}, \mathscr{Q}, \delta)$ where:

- $\mathscr{A}$ is a (nonempty) finite alphabet, i.e., its cardinality $|\mathscr{A}| \in \mathbb{N}$.
- $\mathscr{Q}$ is a (nonempty) finite set of states, i.e., its cardinality $|\mathscr{Q}| \in \mathbb{N}$.
- $\delta : \mathscr{Q} \times \mathscr{A} \to \mathscr{Q}$ is a (deterministic) state transition map.

Definition 2. A symbol block, also called a word, is a finite-length string of symbols belonging to the alphabet $\mathscr{A}$, where the length of a word $w \triangleq s_1 s_2 \cdots s_\ell$ with $s_i \in \mathscr{A}$ is $|w| = \ell$, and the length of the empty word ϵ is $|\epsilon| = 0$. The parameters of FSA are extended as:

- The set of all words, constructed from symbols in $\mathscr{A}$ and including the empty word ϵ, is denoted as $\mathscr{A}^\star$.
- The set of all words, whose suffix (respectively, prefix) is the word w, is denoted as $\mathscr{A}^\star w$ (respectively, $w\mathscr{A}^\star$).
- The set of all words of (finite) length ℓ, where $\ell \in \mathbb{N}$, is denoted as $\mathscr{A}^\ell$.

Remark 2. A symbol string (or word) is generated from a (finite-length) time series by symbolization.

Definition 3. A probabilistic finite state automaton (PFSA) $\mathscr{K}$ is a pair (G, π), where:

- Deterministic FSA G is the underlying algebraic structure of PFSA $\mathscr{K}$.
- The morph function $\pi : \mathscr{Q} \times \mathscr{A} \to [0,1]$ is also known as the symbol generation probability function that satisfies the condition: $\sum_{\sigma \in \mathscr{A}} \pi(q, \sigma) = 1$ for all $q \in \mathscr{Q}$.

Often the state transition probability mass function $\kappa : \mathscr{Q} \times \mathscr{Q} \to [0,1]$ is constructed by combining δ and π, which can be structured as a $|\mathscr{Q}| \times |\mathscr{Q}|$ matrix $\mathscr{T}$. In that case, the PFSA can be described as the triple $\mathscr{K} = (\mathscr{A}, \mathscr{Q}, \mathscr{T})$.

Remark 3. It is noted that the $|\mathscr{Q}| \times |\mathscr{Q}|$ state transition probability matrix $\mathscr{T}$ is stochastic (Berman and Plemmons, 1994) (i.e., each element of $\mathscr{T}$ is non-negative and each row sum is unity). The matrix $\mathscr{T}$ is constructed to be stochastic and ergodic (Berman and Plemmons, 1994), which implies that $\mathscr{T}$ has exactly one eigenvalue at unity (i.e., $\lambda = 1$) and that the rest of the eigenvalues are either on or within the unit circle with center at 0 (i.e., $|\lambda| \leqslant 1$). The (sum-normalized) left eigenvector v corresponding to the unity eigenvalue (i.e., $\lambda = 1$) represents the stationary state probability vector of the Markov chain (Berman and Plemmons, 1994).

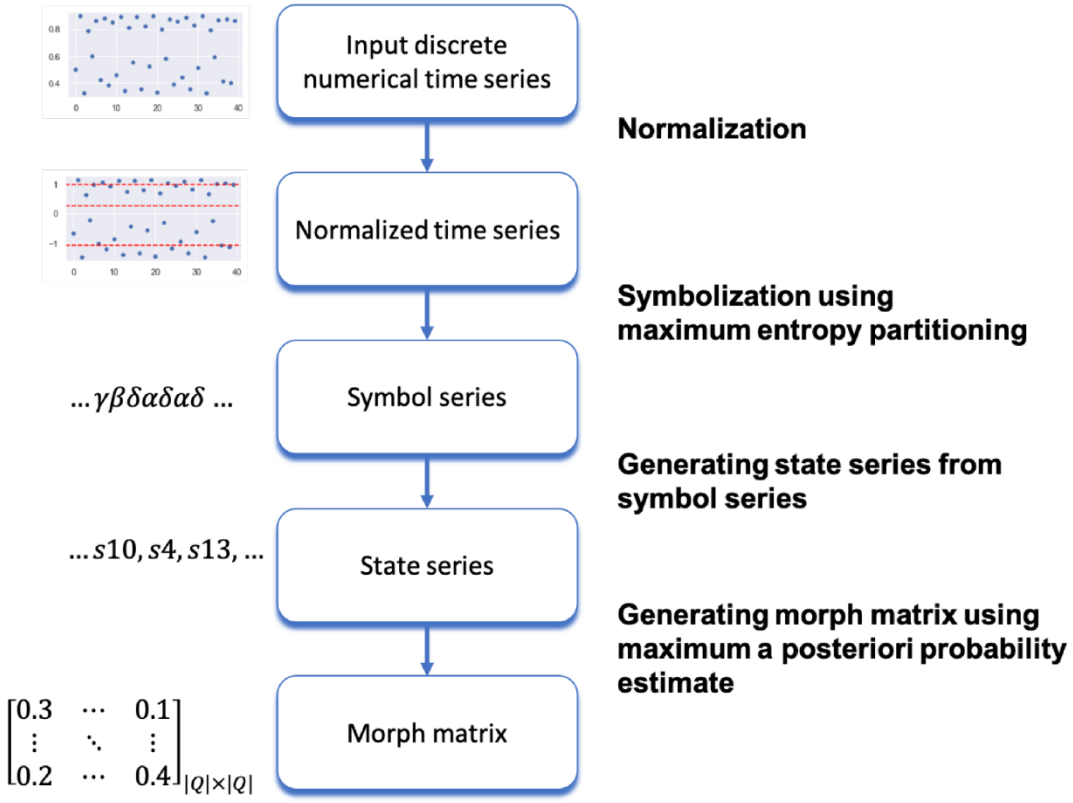

Fig. 5. Flow chart for construction of PFSA.

Remark 4. Construction of the state transition probability matrix $\mathscr{T}$ is a compact way to store the dynamical features, which can be processed by different classifiers to conduct system diagnosis. This representation of $\mathscr{T}$ originates from the inherent characteristic of the state transition pattern of a dynamical system.

3.1. D-Markov Machines

In the construction of a D-Markov machine, it is assumed that the generation of the next symbol depends only on a *finite* history of at most D consecutive symbols, i.e., a symbol block not exceeding the specified length D. In this context, a D-Markov machine (Mukherjee and Ray, 2014) is formally defined as follows.

Definition 4. A D-Markov machine is a PFSA in the sense of Definition 3 and it generates symbols that solely depend on the (most recent) history of at most D consecutive symbols, where the positive integer D is called the *depth* of the machine. Equivalently, a D-Markov machine is a stochastic process $S = \cdots s_{-1}s_0s_1\cdots$, where the probability of occurrence of a new symbol depends only on the last consecutive (at most) D symbols, i.e.,

$$P[s_n|\cdots s_{n-D}\cdots s_{n-1}] = P[s_n|s_{n-D}\cdots s_{n-1}] \tag{26}$$

Consequently, for $w \in \mathscr{A}^D$ (see Definition 2), the equivalence class $\mathscr{A}^\star w$ of all (finite-length) words of suffix w, is qualified to be a D-Markov state that is denoted as w.

Remark 5. While the algebraic structure of the PFSA in D-Markov machines is deterministic (Ray, 2004; Mukherjee and Ray, 2014), a hidden Markov model (HMM) may have a non-deterministic algebraic structure (Dupont et al., 2005; Vidal et al., 2005); this difference yields significant computational advantages of D-Markov machines over HMMs at the expense of limited loss of modeling flexibility. Moreover, since HMMs are typically trained by expectation maximization (Murphy, 2012), the underlying algorithms might suffer from having a poor local optimum. In addition to its iterative computation cost, HMMs may not be sufficiently robust in terms of convergence even to a locally optimum point. In contrast, the deterministic algebraic structure of D-Markov machines makes the modeling process much simpler and less prone to the local optimum issue, where the model can be trained by frequency counting (Mukherjee and Ray, 2014), for example.

The PFSA of a D-Markov machine is capable of generating symbol strings. That is, such a generated symbol string has the form $\{s_1s_2\cdots s_\ell\}$, where $s_j \in \mathscr{A}$ and ℓ is a positive integer. Both morph function π and state probability transition matrix $\mathscr{T}$ implicitly support the fact that PFSA satisfies the Markov condition, where generation of a symbol depends only on the current state that is a symbol string of at most D consecutive symbols (Mukherjee and Ray, 2014).

For construction of the proposed D-Markov-based PFSA, there are four primary choices as enumerated below:

1. **Alphabet size ($|\mathscr{A}|$)**: Larger is the alphabet size, the dynamical system is more discretely represented as different symbols, which will require more training data. Therefore, selection of the alphabet $\mathscr{A}$ is a critical step of PFSA construction.
2. **Partitioning Method**: While there are many data partitioning techniques, such as maximum entropy partitioning (MEP) and uniform partitioning (Rajagopalan and Ray, 2006; Subbu and Ray, 2008) and K-means partitioning (Murphy, 2012), the selection of the partitioning method is largely problem-specific. The symbolization in this paper has been conducted through MEP, where the number of data points in each partitioning segment are the same so that the entropy is maximized.
3. **Depth (D) in the D-Markov machine**: In this paper, $D = 1$ has been primarily chosen for PFSA construction to limit the window length L. Higher values of the positive integer D may lead to better results at the expense of increased number of states $|\mathscr{Q}|$ and CPU time due to

larger dimension of the feature space and thus may need more training data.

4. **Choice of Feature**: The feature needs to be the one that best captures the physical nature (e.g., texture) of the signal and also that is not computationally too expensive. In this paper, the (absolute sum-normalized) principal left eigenvector of the $\mathscr{T}$-matrix is selected as feature.

Fig. 5 depicts the flow chart of PFSA construction. It starts from symbolization of the normalized numerical time series (e.g., the neutron noise time-series data in this work). After partitioning, each interval is labeled by a unique symbol. Then the numerical time series is transformed into a symbol string. Based on the symbol string, the Markov model is generated by sliding through the symbol string with a given window length. Finally a state transition probability matrix $\mathscr{T}$ is constructed by counting the state transitions. A pseudo-code of the PFSA training algorithm is presented below.

Algorithm 1: PFSA training algorithm

Input: Alphabet size $|\mathcal{A}|$, Markov depth D, observed time series S
Result: State transition probability matrices $\mathcal{T}^{(i)}$ for each class i out of N classes
Determine the upper bound and lower bound of S;
Generate partitioning boundaries according to $|\mathcal{A}|$ and the bounds;
Symbolize the time series S using the partitioning boundaries;
Generate the state sequence for each symbol string according to the Markov depth D;
for $i \leftarrow 1$ **to** N **do**
  initialize state transition probability matrices $\mathcal{T}^{(i)}$;
  for $j \leftarrow 0$ **to** *the end of each symbol string s, in the class i* **do**
    $\mathcal{T}^{(i)}_{s_j,s_{j+1}} \leftarrow \mathcal{T}^{(i)}_{s_j,s_{j+1}} + 1$;
  end
  normalize $\mathcal{T}^{(i)}$ in each row;
end

3.2. Classification of the Health Condition

Given that the state transition matrix $\mathscr{T}$ is constructed to be both stochastic and ergodic (Mukherjee and Ray, 2014), each element of the left eigenvector (v^0) of $\mathscr{T}$, associated with the (unique) eigenvalue 1, is non-zero and is of the same sign. Therefore, after sum-normalization, v^0 represents the state probability distribution of the PFSA and is selected as a feature vector for the time series from which the PFSA is constructed.

If two time series belong to the same class, the corresponding feature vectors (i.e., v^0) should be very similar; otherwise these two feature vectors would point to different directions signifying that the two respective time series belong to different classes. For example, let there be only two possible classes: the nominal class C_{nom} and the faulty class C_{flt}. Then, the residual error between the nominal feature v^0_{nom} and the test feature v^0_{tst}, which may belong to either C_{nom} or C_{flt}, is given as:

$$\varepsilon_{nom} \triangleq d\left(v^0_{nom}, v^0_{tst}\right) = \left\| \left(v^0_{nom}\right)^{\mathrm{T}} \left(v^0_{nom} \left(v^0_{nom}\right)^{\mathrm{T}} \right)^{-1} v^0_{nom} \left(v^0_{tst}\right)^{\mathrm{T}} \right\|. \tag{27}$$

Similarly, the residual error between the faulty feature, v^0_{flt}, and the test feature v^0_{tst}, which also may belong to either C_{nom} or C_{flt}, is given as:

$$\varepsilon_{flt} \triangleq d\left(v^0_{flt}, v^0_{tst}\right) = \left\| \left(v^0_{flt}\right)^{\mathrm{T}} \left(v^0_{flt} \left(v^0_{flt}\right)^{\mathrm{T}} \right)^{-1} v^0_{flt} \left(v^0_{tst}\right)^{\mathrm{T}} \right\|, \tag{28}$$

where Eqs. (27) and (28) are the norms of the test vector v^0_{tst} projected onto the orthogonal directions of the features v^0_{nom} and v^0_{flt}, respectively. The class label (which is either 'nominal' or 'faulty' in this example) is then determined by:

$$\text{Identified Class} = \operatorname{argmin}\left\{\varepsilon_{nom}, \varepsilon_{flt}\right\}. \tag{29}$$

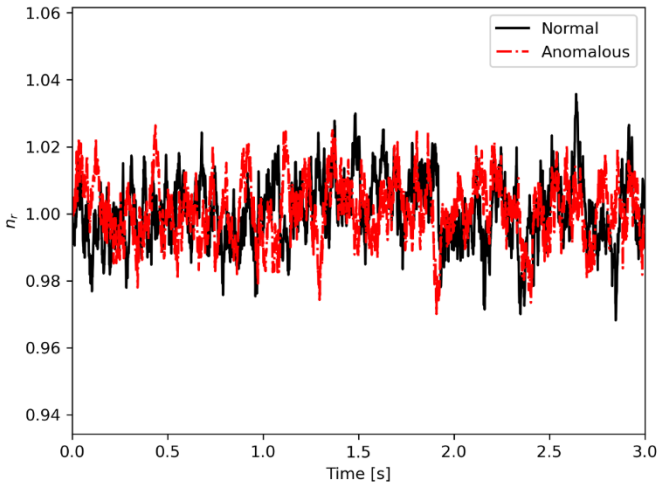

(a) In-core signal

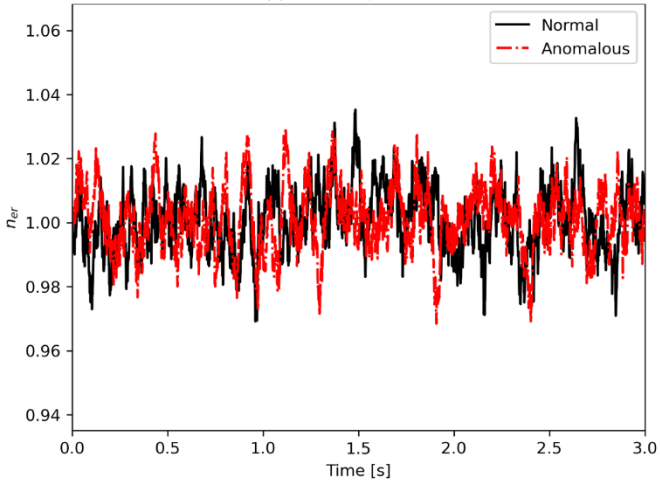

(b) Ex-core signal

Fig. 6. Typical time series of neutron noise in the first 3 s.

In practice, not all anomaly conditions could be known before they happen; thus, the anomaly identification may not always be possible. However, an anomaly should be detected even though it may not be identified immediately. It will be even more beneficial, if the anomaly is at its early stage (e.g., no excessive vibration). In this case, a threshold on the residual error to the nominal feature vector can be used for discrimination. Since this case bears similar discrimination criteria, it is not used here to avoid repetition. Instead, a two-class discrimination is reported, where the first class is the normal condition, belonging to C_{nom}, and the second class is the anomalous condition belonging to C_{flt}, caused by abnormal vibration of the fuel assembly, for example.

4. Results and Discussion

This section reports the results of anomaly detection (see Section 3) from an ensemble of time series, generated from the models developed in Section 2. The normal and amonalous cases of the fuel assembly vibrations are the ones given in SubSection 2.2. To be specific, the normal case has the fuel assembly displacement depicted by Eq. (12) while the anomalous vibration is represented by Eqs. (9)–(11) where the $[A_1, A_2, A_3, A_4] = [10, -50, 0, 100]$ and $A_i = 0$ for $i > 4$. The source codes of the developed model and PFSA are available online [2].

[2] https://github.com/chenxiangyi10/neutronNoisePFSA.

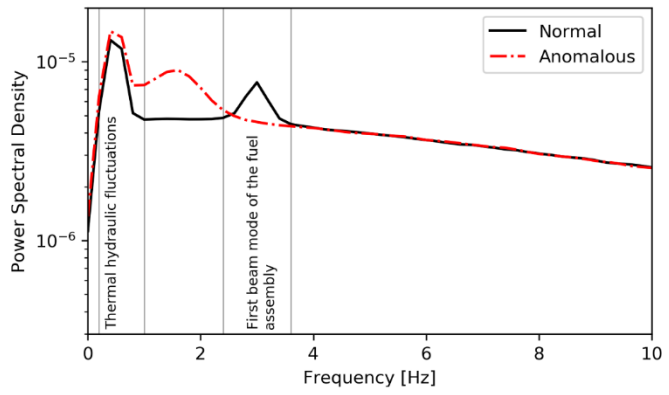

(a) In-core detector.

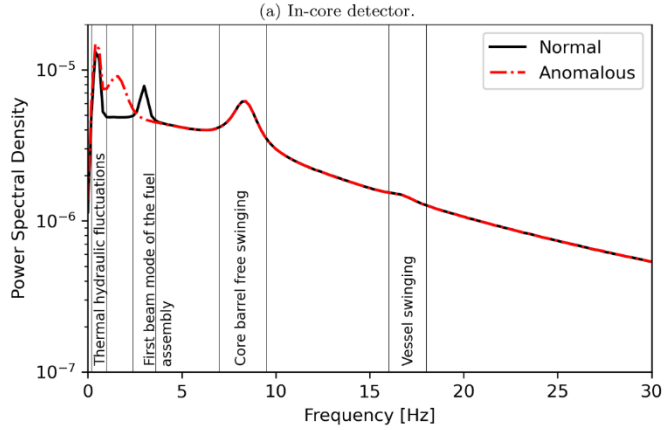

(b) Ex-core detector.

Fig. 7. Typical PSD of neutron noise from in-core detector and ex-core detector.

4.1. Time series data generation

The models, constructed in Section 2, have been used to generate in-core and ex-core signals with and without fuel assembly vibration anomaly. The forward Euler's method with a step size of 0.001 s has been used in the model equations for all simulation runs. This step size has been confirmed to have less than around 0.1% error compared with using 1×10^{-6} second step size which is acceptable for both simulating the time series trajectory and quantifying the performance of the PFSA. One billion steps are simulated to account for 1 million seconds (around 11.5 days) for both nominal and anomalous conditions. Fig. 6 presents the first 3 s of the signals detected by both in-core and ex-core detectors. The difference of the signatures detected by different detectors and the health condition are barely visible, unless viewing the signals in frequency domain, which are shown in Figs. 7 (a) and 7 (b). Distinct peaks are absent in the PSD of the in-core detector, but they are present in the PSD of the ex-core detector, as explained in SubSection 2.3.

4.2. Data processing for pattern classification

The time series data are divided into training and test sets by using different window lengths that are: [10, 20, 40, 80, 100, 200, 400, 800, 1,000] in the unit of seconds. It should be noted that the developed model is stationary (Stein and Dubi, 2020) and ergodic (i.e., Cauchy sequences of time-averages converge to the respective ensemble averages in a stochastic sense (Durrett, 2010)). Thus, sampling by windows from one realization is valid to test the PFSA algorithm; otherwise, multiple trajectories should be generated for testing. It is recalled that the time step interval in the simulation is 0.001 s so that the frequency of sampling (fs) is 1,000 Hz. To investigate the effects of the sampling frequency on the performance of PFSA, the original time series is downsampled to 10 Hz and 100 Hz from the original frequency of 1,000 Hz.

4.3. Results of PFSA-based anomaly detection

Fig. 8 depicts the performance of PFSA under different hyper-parameters of window length L and alphabet size $|\mathscr{A}|$. The performance is characterized by the accuracy of the binary classification, which is the number of correct predictions divided by total number of predictions. It is seen that the in-core detector is more suitable for fuel assembly detection. This observation is reasonable, because it does not contain the high-frequency components of the fluctuating signals in the core barrel and pressure vessel, thus less noisy. The accuracy improves by increasing the window length, and it reaches around 100% when the window length is greater than 800 s, as seen in Fig. 8(a). The accuracy also increases when the partitioning cells are made denser (i.e., the alphabet size $|\mathscr{A}|$ is increased). This is seen in Fig. 8(b), which uses the alphabet size $|\mathscr{A}|$ of [5, 10, 20, 40, 50, 60, 70, 80, 100, 150, 200, 400, 800]. However, the accuracy does not increase significantly after $|\mathscr{A}|$ exceeds 50.

Fig. 9 shows the effects of frequency of sampling rate on the performance of PFSA, where the performance is largely similar for fs $= 100$ Hz and $1,000$ Hz. The former one just has a little lower accuracy; however, when fs $= 10$ Hz, the accuracy is substantially lower. This is explained by the aliasing effect, because the frequency of the dominant signal is under 20 Hz and the fuel assembly is vibrating at ~ 3 Hz, which

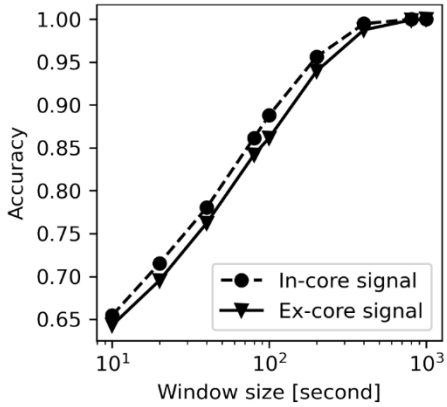

(a) Accuracy versus window length, the alphabet size $|\mathcal{A}|$ is 50.

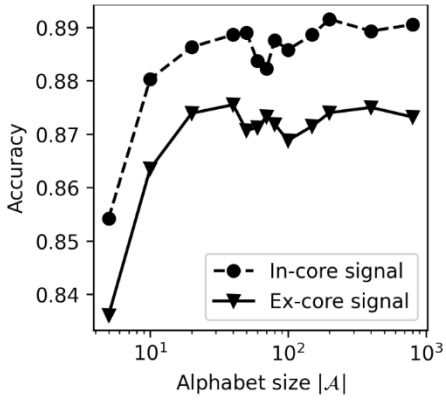

(b) Accuracy versus alphabet size $|\mathcal{A}|$, the window length is 100 seconds.

Fig. 8. Accuracy of in-core and ex-core signals at fs = 1000 Hz.

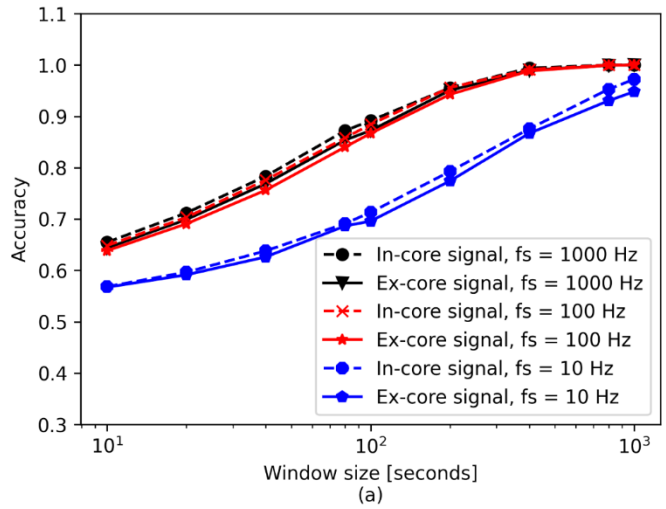

Fig. 9. Accuracy of in-core and ex-core test signals: the accuracy versus window length at different frequency of sampling, the alphabet size $|\mathscr{A}| = 50$ for all cases.

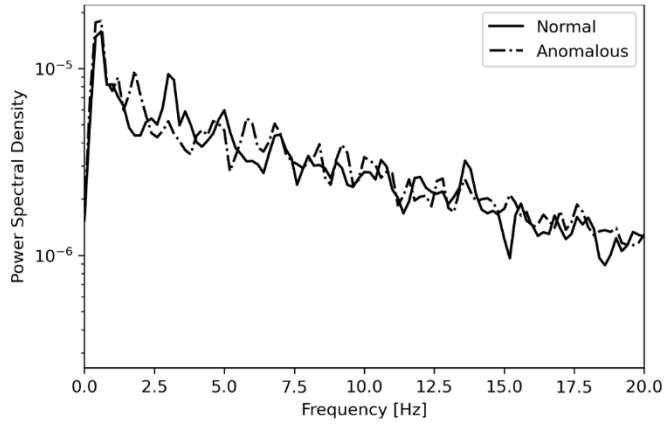

Fig. 10. The PSDs of the nominal neutron time series and anomalous time series of the in-core detector estimated by Welch's method with window length of 100 s, frequency of sampling 100 Hz, number per segment 500; the PFSA alphabet size $|\mathscr{A}|$ is 50.

is not much lower than 10 Hz. Fig. 10 shows an example of PSDs of the neutron noise with fs $= 100$ Hz and window length of 100 s. It is seen that these PSDs are noisy for short windows, at which PFSA can achieve an accuracy of $\sim 88.8\%$.

A concatenated time series of the normal and anomalous time series has been used here for demonstration of PFSA performance. During the first 9,000 s, the fuel assembly is under the normal condition. The anomaly starts at the time instant of 9,000 s and is continued to the end. Fig. 11 shows the results of PFSA for online anomaly detection, where '1' means that PFSA classifies the system to be under an abnormal condition, while '0' means the normal condition. The residual errors are shown in green-color and blue-color curves for normal and anomalous conditions, respectively. The vertical red line shows the time when anomaly first occurred where the window length is 1,000 s and the alphabet size $|\mathscr{A}|$ is 50. The subplot Fig. 11(a) shows absence of false alarms before the anomaly occurs. The first alarm of anomaly is triggered at 524 s after the anomaly actually occurred, as detailed in the subplot Fig. 11(b). This delay time is around half of the window length, when a major part of time series in the window interval shifts from the normal to an anomalous condition. Once the first anomaly is detected, there is no further missed alarms.

5. Summary, Conclusions, and future work

This paper has developed a neutron noise model to generate ensembles of time series data for anomaly detection in reactor internals. The objectives here are the following:

- Mimicking the power spectral density (PSD) of observed neutron noise in real-life nuclear power plants.
- Generation of simulated time series of neutron power under both normal and abnormal conditions of reactor operation based on a low-order model.
- Symbolization of time series of simulated neutron power to generate symbol strings.
- Construction of probabilistic finite state automata (PFSA) models of neutron noise dynamics from symbol strings.
- Detection of anomalies in the reactor based on the above PFSA models.

The results show that the PFSA-based pattern classification is capable of detecting anomalies with high accuracy when the frequency spectra are noisy as well as for short-length windows. The PFSA algorithms can also generate consistent alarms if the window length is made sufficiently large. It is demonstrated that the PFSA-based pattern classification has the potential to serve both quantitatively and qualitatively as an important tool for anomaly detection in reactor internals.

While there are many areas of theoretical and experimental research to enhance the work reported in this paper, the authors suggest the following topics for future research:

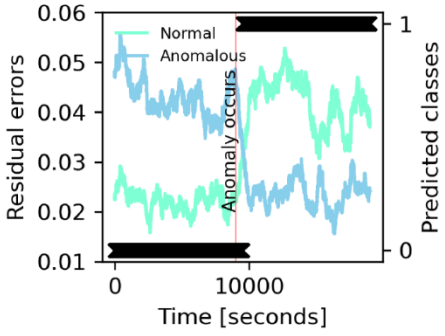

(a) Predicted classes and residual errors vs. time. (Vertical red line ≡ anomaly occurrence.)

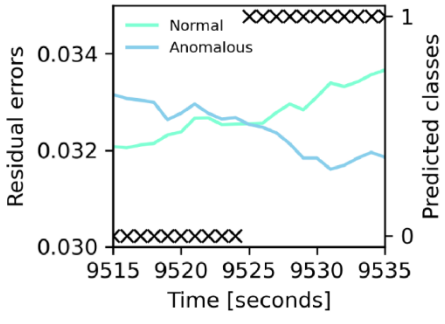

(b) Zoom-in of subplot (a) in the time interval when the anomaly is detected.

Fig. 11. Online anomaly detection.

1. Demonstration of the PFSA concept on an ensemble of data collected from an operating PWR.
2. Application of the PFSA algorithms to other signatures collected in PWRs for anomaly detection and identification.
3. Deployment of the PFSA algorithms for online anomaly detection to investigate the computational cost and limitations of this methodology for real-life applications.
4. Extension of the PFSA-based anomaly detection for fault-tolerant decision & control of nuclear power plants under different strategies.

CRediT authorship contribution statement

Xiangyi Chen: Conceptualization, Methodology, Software, Writing - original draft. **Asok Ray:** Supervision, Methodology, Writing - original draft. **Fan Zhang:** Methodology, Writing - original draft.

Declaration of Competing Interest

The authors declare that they have no known competing financial interests or personal relationships that could have appeared to influence the work reported in this paper.

References

Alguindigue, I., Uhrig, R.E., Cai, M., Trenty, A., 1993. Discrimination of ex-core neutron noise signatures using artificial neural networks. Technical Report. Electricite de France (EDF).

Berman, A., Plemmons, R., 1994. Nonnegative Matrices in the Mathematical Sciences. SIAM Press, Philadelphia, PA, USA.

X. Chen, A. Ray, On singular perturbation of neutron point kinetics in the dynamic model of a pwr nuclear power plant, Sci: An MDPI Journal (ISSN 2413–4155) 36 (May 2020). doi: 10.3390/sci2020036.

Chionis, D., Dokhane, A., Belblidia, L., Ferroukhi, H., Girardin, G., Pautz, A., 2020. Development and verification of a methodology for neutron noise response to fuel assembly vibrations. Annals of Nuclear Energy 147, 107669.

Demaziere, C., 2011. Core sim: A multi-purpose neutronic tool for research and education. Annals of Nuclear Energy 38, 2698–2718.

C. Demazière, A. Mylonakis, P. Vinai, A. Durrant, F.D.S. Ribeiro, J. Wingate, G. Leontidis, S. Kollias, Neutron noise-based anomaly classification and localization using machine learning, in: EPJ Web of Conferences, volume 247, EDP Sciences, 2021, p. 21004.

Dubi, C., Atar, R., 2021. Modeling reactor noise due to rod and thermal vibrations with thermal feedback using stochastic differential equations. Nuclear Science and Engineering 195, 256–270.

Dupont, P., Denis, F., Esposito, Y., 2005. Links between probabilistic automata and hidden Markov models: probability distributions, learning models and induction algorithms. Pattern Recognition 38, 1349–1371.

Durrant, A., Leontidis, G., Kollias, S., 2019. 3d convolutional and recurrent neural networks for reactor perturbation unfolding and anomaly detection. EPJ Nuclear Sciences & Technologies.

A.M. Durrant, G. Leontidis, S. Kollias, A. Torres, C. Montalvo, A. Mylonakis, C. Demaziere, P. Vinai, Detection and localisation of multiple in-core perturbations with neutron noise-based self-supervised domain adaptation (2021).

Durrett, R., 2010. Probability: Theory and Examples, Cambridge Series in Statistical and Probabilistic Mathematics, 4 ed.,.

Edwards, R.M., Lee, K.Y., Schultz, M., 1990. State feedback assisted classical control: an incremental approach to control modernization of existing and future nuclear reactors and power plants. Nuclear technology 92, 167–185.

Ghalyan, N.F., Ray, A., 2020. Symbolic time series analysis for anomaly detection in measure-invariant ergodic systems. Journal of Dynamic Systems, Measurement, and Control 142, 061003.

Ghalyan, N.F., Ray, A., 2021. Measure invariance of ergodic symbolic systems for low-delay detection of anomalous events. Mechanical Systems and Signal Processing 159, 107746.

Kim, K.-T., Suh, J.-M., 2008. Development of an advanced pwr fuel for opr1000s in korea. Nuclear Engineering and Design 238, 2606–2613.

Konno, H., 1986. The stochastic process of non-linear random vibration: Reactor-noise analysis of hump phenomena in a time domain. Annals of Nuclear Energy 13, 185–201.

Konno, H., Saito, K., 1984. Effect of a local non-linear vibration on the space-time behaviour of the neutron field in nuclear reactors. Annals of Nuclear Energy 11, 1–13.

H. Konno, Nonlinear stochastic theory and identification of nonlinearity in nuclear reactors, in: Noise and Nonlinear Phenomena in Nuclear Systems, Springer, 1989, pp. 179–192.

Krapf, D., Marinari, E., Metzler, R., Oshanin, G., Xu, X., Squarcini, A., 2018. Power spectral density of a single brownian trajectory: what one can and cannot learn from it. New Journal of Physics 20, 023029.

Lee, I.S., Yu, Y.H., Son, H.M., Hwang, J.S., Suh, K.Y., 2006. Natural convection heat transfer in a rectangular liquid metal pool with bottom heating and top cooling, in. International Conference on Nuclear Engineering 42436, 141–148.

R.M. Meyer, J.B. Coble, E.H. Hirt, P. Ramuhalli, M.R. Mitchell, D.W. Wootan, E.J. Berglin, L.J. Bond, C.H. Henager, Technical needs for prototypic prognostic technique demonstration for advanced small modular reactor passive components, Technical Report, Pacific Northwest National Lab. (PNNL), Richland, WA (United States), 2013.

Mukherjee, K., Ray, A., 2014. State splitting and merging in probabilistic finite state automata for signal representation and analysis. Signal processing 104, 105–119.

Murphy, K., 2012. Machine Learning: A Probabilistic Perspective. The MIT Press, Cambridge, MA, USA.

Preumont, A., 2013. Random Vibration and Spectral Analysis/Vibrations aléatoires et analyse spectral, volume 33. Springer Science & Business Media.

Rajagopalan, V., Ray, A., 2006. Symbolic time series analysis via wavelet-based partitioning. Signal Processing 86, 3309–3320.

Ray, A., 2004. Symbolic dynamic analysis of complex systems for anomaly detection. Signal Processing 84, 1115–1130.

H. Schoonewelle, T. Van der Hagen, J. Hoogenboom, Application of process-monitoring techniques to neutron noise signals from simulated-coolant-boiling experiments, in: Proc. Int. Conf. INCORE, volume 96, 1996, pp. 16–20.

Seidl, M., Kosowski, K., Schüler, U., Belblidia, L., 2015. Review of the historic neutron noise behavior in german kwu built pwrs. Progress in Nuclear Energy 85, 668–675.

Shieh, D., Upadhyaya, B., Sweeney, F., 1987. Application of noise analysis technique for monitoring the moderator temperature coefficient of reactivity in pressurized water reactors. Nuclear science and engineering 95, 14–21.

Singiresu, S.R., et al., 1995. Mechanical vibrations. Addison Wesley Boston, MA.

Stein, G., Dubi, C., 2020. Stabilization of the stochastic point reactor kinetic equation through power feedback. The European Physical Journal Plus 135, 1–14.

Subbu, A., Ray, A., 2008. Space partitioning via hilbert transform for symbolic time series analysis. Applied Physics Letters 92, 084107.

Thie, J.A., 1979. Core motion monitoring. Nuclear Technology 45, 5–45.

Torres, L., Chionis, D., Montalvo, C., Dokhane, A., García-Berrocal, A., 2019. Neutron noise analysis of simulated mechanical and thermal-hydraulic perturbations in a pwr core. Annals of Nuclear Energy 126, 242–252.

Trenty, A., Puyal, C., Klajnmic, H., 1991. SINBAD, a data base for PWR internals vibratory monitoring. Technical Report. Electricite de France (EDF).

Vidal, E., Thollard, F., de la Higuera, C., Casacuberta, F., Carrasco, R., 2005. Probabilistic finite-state machines - Part I and Part II. IEEE Transactions on Pattern Analysis and Machine Intelligence 27, 1013–1039.

Viebach, M., Lange, C., Kliem, S., Demaziere, C., Rohde, U., Hennig, D., Hurtado, A., 2019. A comparison between time domain and frequency domain calculations of stationary neutron fluctuations. In: Proc. Int. Conf. Mathematics and Computational Methods Applied to Nuclear Science and Engineering (M&C 2019), pp. 25–29.

Welch, P., 1967. The use of fast fourier transform for the estimation of power spectra: a method based on time averaging over short, modified periodograms. IEEE Transactions on audio and electroacoustics 15, 70–73.

Zwingelstein, G., Upadhyaya, B., 1979. Identification of multivariate models for noise analysis of nuclear plant. IFAC Proceedings Volumes 12, 1301–1307.